Robotica (2025), **43**, pp. 1491–1511
doi:10.1017/S0263574725000384

CAMBRIDGE UNIVERSITY PRESS

RESEARCH ARTICLE

Improving machining trajectory accuracy for dual-robot system with in situ laser measurement and meta-heuristic optimization

Zhentao Zhang[1], Guangde Bi[1], Jiajing Li[1], Lining Sun[1,2] and Lei Lu[1]

[1]Jiangsu Provincial Key Laboratory of Advanced Robotics & Collaborative Innovation Center of Suzhou Nano Science and Technology, Soochow University, Suzhou, China
[2]State Key Laboratory of Robotics and System, Harbin Institute of Technology, Harbin, China
Corresponding author: Lei Lu; Email: lulei@suda.edu.cn

Received: 27 November 2024; **Revised:** 27 February 2025; **Accepted:** 1 March 2025; **First published online:** 2 April 2025

Keywords: measurement-machining robot system; in situ laser measurement; robot calibration; robot machining trajectory improvement; meta-heuristic optimization method

Abstract

Industrial robots are widely utilized in the machining of complex parts because of their flexibility. However, their low positioning accuracy and spatial geometric error characteristics significantly limit the contour precision of robot machined parts. Therefore, in the robot machining procedure, an in situ measurement system is typically required. This study aims to enhance the trajectory accuracy of robotic machining through robotic in situ measurement and meta-heuristic optimization. In this study, a measurement-machining dual-robot system for measurement and machining is established, consisting of a measurement robot with a laser sensor mounted at the robot end and a machining robot equipped with a machining tool. In the measuring process, high-precision standard spheres are set on the edge of the machining area, and the high-precision standard geometry is measured by the measurement robot. According to measured geometry information in the local area, the trajectory accuracy for the machining robot is improved. By utilizing the standard radius of the standard spheres and adopting a meta-heuristic optimization algorithm, this study addresses the complexity of the robot kinematics model, while also overcoming local optima commonly introduced by gradient-based iterative methods. The results of the experiments in this study confirm that the proposed method markedly refines the precision of the robot machining trajectory.

1. Introduction

Industrial robots are widely utilized for difficult machining parts due to their larger workspace and flexibility [1–6]. Dual-robot systems are widely utilized across various fields, such as machining [7–9], assembly [10–13], and so on. In a dual-robot system, one robot could be equipped with sensors (e.g., cameras and laser sensors), while the other is equipped with machining end-effectors (e.g., milling tools and grinding tools), which form a measurement-machining dual-robot system. This configuration constitutes a measurement-machining dual-robot system that leverages measurement data to enhance the precision of machining trajectory operations.

However, low trajectory accuracy of the robot limits the quality of surface machining in tasks such as robot milling or grinding. Many researchers have approached this issue from various perspectives, proposing methods to improve the trajectory accuracy of robots. Wu et al. [14] proposed a method based on iterative learning to design a high-precision feedforward controller, which reduces errors caused by dynamic effects. Maghami et al. [15] introduced a vision-based robot pose correction technique that enhances the accuracy of robotic drilling operations. Tao et al. [16] employed a BLL residual prediction network for error compensation in the robot's inverse kinematics model, improving model accuracy. Wu et al. [17] demonstrated that adding an extra leg can improve the stiffness and natural frequency of

© The Author(s), 2025. Published by Cambridge University Press.

https://doi.org/10.1017/S0263574725000384 Published online by Cambridge University Press

a 3-DOF parallel manipulator, enhancing positioning accuracy and motion stability through optimized robot configuration.

To enable the dual-robot system to execute designated tasks with high precision, system calibration is essential. However, the calibration issues associated with dual-robot systems are varied and intricate. Many researchers have conducted studies on this topic. Wang et al. [18] formalized a class of problems in dual-robot systems as AXB = YCZ. This formula has provided a broad foundation for subsequent researchers, inspiring numerous studies in the field. Wu et al. [19] proposed a method for simultaneously calibrating multiple sets of relative position and orientation relationships within a dual-robot system, which alleviates the error accumulation caused by traditional asynchronous calibration methods. Sui et al. [20] solved AXB = YCZ problem by using geometric algebra-based and geometric calculus-based techniques. Qiao et al. [21] presented a model grounded in the product of exponentials formula, which eliminates the reliance on nominal kinematic parameters. This results in a significant reduction of the robot's end-effector position error to 0.8563 mm.

Most of the researches on the dual-robot system calibration focus on the global motion range of the robots, which makes it challenging to improve the repeatability and positioning accuracy for a certain machining trajectory. Recently, methods for local calibration within the machining area have sparked extensive research. Many researchers have applied these methods to the calibration of various systems. Nubiola et al. [22] performed calibration of an ABB IRB 1600 robot within a 0.7 m^3 workspace, achieving a positioning error reduction to 0.292 mm. Xu et al. [23] proposed a tool center point-based calibration technique within designated local workspace. This method achieves an impressive accuracy of 0.132 mm. Wang et al. [24] utilized spherical constraints to calibrate robot end-effectors. This method improved the positioning precision of the robot by 90%. Dehghani et al. [25] proposed a method for calibrating the kinematic parameters of the robot machining system, which improved the tool path accuracy to 0.15 mm within the specified operational area.

Studies about calibration and trajectory improvement often involve nonlinear optimization problems. Meta-heuristic algorithms demonstrate strong capabilities in escaping local optima and show broad applicability in solving the problems. Many researchers have employed meta-heuristic algorithms in the field of robot calibration and achieved promising results. Chen et al. [26] proved that the Hybrid-of-Evolutionary-Schemes model they introduced could reduce position errors in the industrial robot while maintaining high computational efficiency. Cao et al. [27] utilized a neural network based on a butterfly and flower pollination algorithm to enhance the accuracy of robot calibration. Chen et al. [28] proposed an improved beetle swarm optimization algorithm to enhance the trajectory accuracy of drilling robots. Zhong et al. [29] improved kinematic calibration accuracy of a segmented hydraulic leg system based on an improved whale swarm algorithm. However, none of these researches apply the meta-heuristic algorithm in dual-robot calibration.

This paper proposes a novel method for improving the trajectory accuracy of a dual-robot system through local space calibration and the use of a meta-heuristic algorithm. The objective is to correct the theoretical kinematic model of the robot through dual-robot calibration within a localized region. This aims to enhance the trajectory accuracy of the end-effector within its operational area. Additionally, a meta-heuristic algorithm, Electric Eel Foraging Optimization algorithm (EEFO) [30], is leveraged to avoid local optima, thereby improving calibration precision. To verify the proposed method, an Archimedean spiral line and a sine surface have been machined by the dual-robot system in this study. The machining results show a significant improvement in trajectory precision.

2. Overview of the measurement-machining robot system

The in situ measurement and machining robot system designed in this study is shown in Fig. 1. The system includes a robot with a high-precision laser sensor mounted at the end, another robot with ball-end milling cutter attached at the end, and a fixture equipped with four standard spheres. Both robots are equipped with six degrees of freedom. This design aims to expand the reachable space of both robots and increase the range of available poses, enabling the system to measure and machine complex parts.

https://doi.org/10.1017/S0263574725000384 Published online by Cambridge University Press

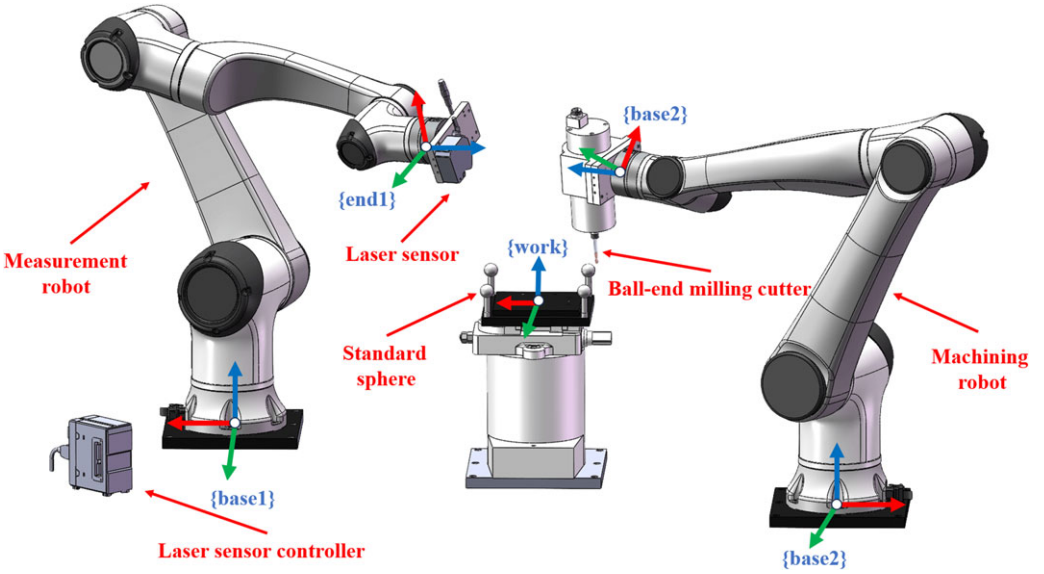


Figure 1. *Overview of the experimental platform.*

Before machining, it is necessary to establish the kinematic relationship between the two robots and calibrate their kinematic parameters. During the actual machining of specific parts, considering their geometry, fine-tuning of the workpiece coordinate system's position and pose is often required. Therefore, in each machining task, the measurement robot is used to obtain the position and pose of the workpiece coordinate system, which are transformed to machining side for machining. The workflow of the dual-robot platform proposed in this study is divided into a calibration stage and a machining stage.

During the calibration stage, both robot end-effectors are equipped with laser sensors to measure four standard spheres within the same workpiece coordinate system, collecting a large amount of geometry data of the standard spheres. Using this data and the EEFO algorithm, the kinematic model for each individual robot is calibrated. Finally, the co-workpiece coordinate system serves as a reference to establish the relationship between the base coordinate systems of the two robots. At this point, both the relationship between the two robots and the kinematic parameters of each robot have been calibrated. The flowchart of the calibration stage is shown in Fig. 2.

Due to the particularities of the workpieces in each machining instance, adjustments to the position and pose of the workpiece coordinate system are often required. Consequently, the recalibration of its position and pose relative to the machining robot is necessary for each production cycle. In this paper, the measurement robot first measures four standard spheres around the newly adjusted workpiece. The EEFO algorithm is then applied to optimize the kinematic relationship between the new workpiece coordinate system and the two robots. Utilizing the relationship between measurement-machining robot established during the calibration stage, the position and pose of the workpiece coordinate system relative to the base coordinate system of the machining robot are obtained. As a result, the accuracy of the machining robot system is enhanced, and the joint trajectories can be generated based on the calibrated kinematic model of the robot system. The flowchart of the calibration stage is shown in Fig. 3.

3. The theoretical kinematic model of the measurement-machining robot system

3.1 The theoretical kinematic model of the measurement robot

As shown in Fig. 4, the measurement robot is illustrated, where coordinate systems are established for the robot base, flange, laser sensor, and workpiece. In this figure, {base1} is the base coordinate system of the measurement robot. {end1} denotes the flange coordinate system. {laser} refers to the coordinate

https://doi.org/10.1017/S0263574725000384 Published online by Cambridge University Press

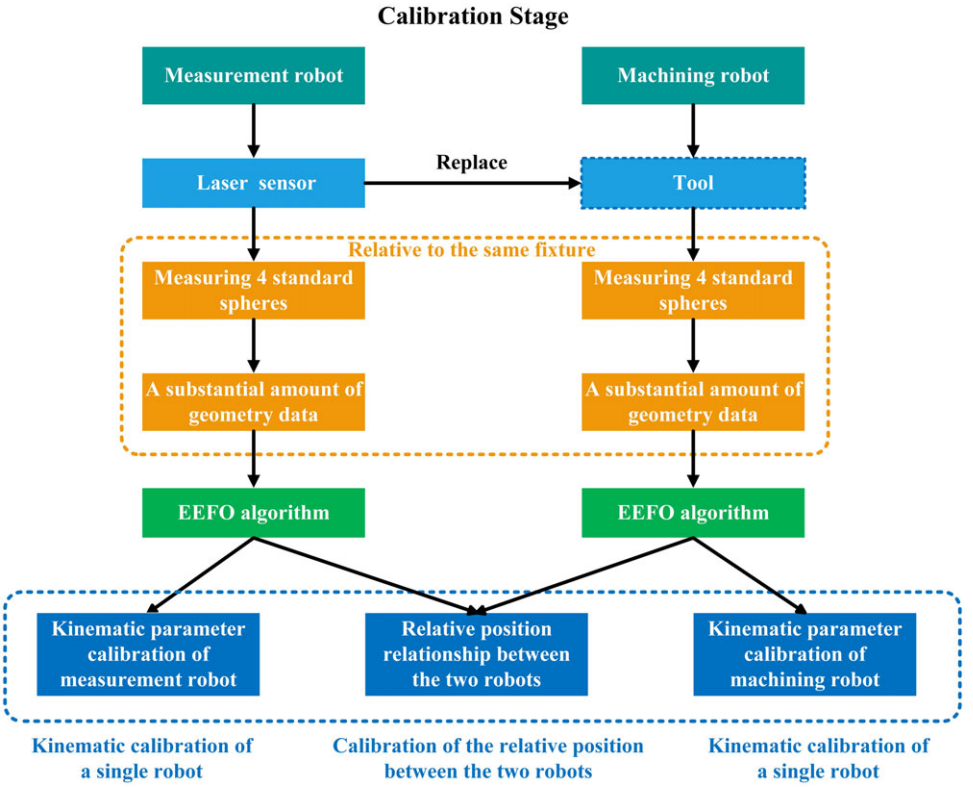


Figure 2. *The flowchart of the calibration stage.*

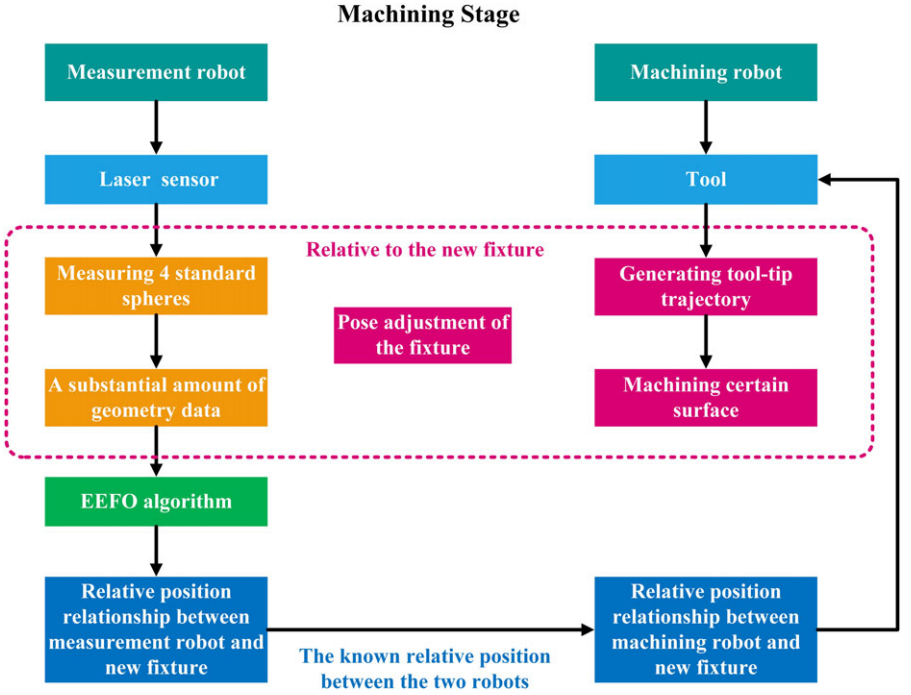


Figure 3. *The flowchart of the machining stage.*

https://doi.org/10.1017/S0263574725000384 Published online by Cambridge University Press

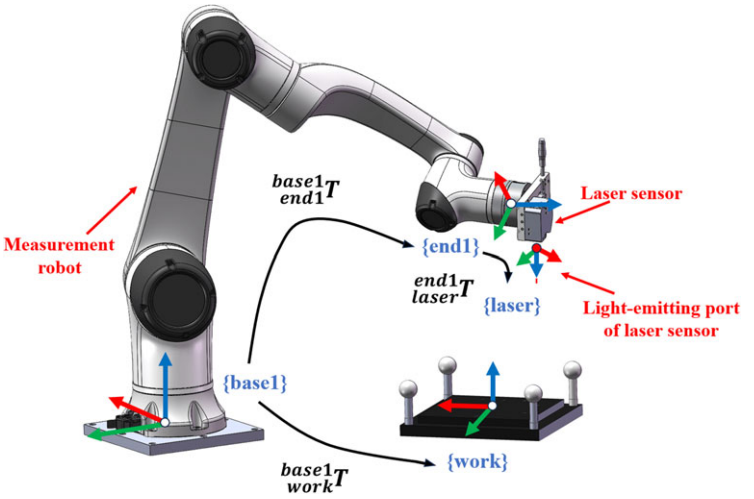


Figure 4. *The theoretical kinematic model of the measurement robot.*

system of the laser sensor, with its origin at the light-emitting port of the sensor. {work} indicates the workpiece coordinate system, and its origin is at the geometric center of the square fixture.

${}^{base1}_{work}T$ denotes the transformation matrix from {base1} to {work} and is defined as

$$ {}^{base1}_{work}T = {}^{base1}_{work}T_P \cdot Rot_z(R_z) \cdot Rot_y(R_y) \cdot Rot_x(R_x) \tag{1} $$

In this equation, ${}^{base1}_{work}T_P$ is defined as

$$ {}^{base1}_{work}T_P = \begin{bmatrix} 1 & 0 & 0 & X_{work} \\ 0 & 1 & 0 & Y_{work} \\ 0 & 0 & 1 & Z_{work} \\ 0 & 0 & 0 & 1 \end{bmatrix} \tag{2} $$

${}^{base1}_{work}T$ contains three rotation variables R_x, R_y, R_z and three position variables X_{work}, Y_{work}, Z_{work}.

${}^{end1}_{laser}T$ denotes the homogeneous transformation matrix from {end1} to {laser} and is defined as

$$ {}^{end1}_{laser}T = {}^{end1}_{laser}T_P \cdot Rot_z(r_z) \cdot Rot_y(r_y) \cdot Rot_x(r_x) \tag{3} $$

In this equation, ${}^{end1}_{laser}T_P$ represents the position of the laser sensor's origin in {end1} and is defined by the following homogeneous matrix:

$$ {}^{end1}_{laser}T_P = \begin{bmatrix} 1 & 0 & 0 & X_{laser} \\ 0 & 1 & 0 & Y_{laser} \\ 0 & 0 & 1 & Z_{laser} \\ 0 & 0 & 0 & 1 \end{bmatrix} \tag{4} $$

${}^{end1}_{laser}T$ contains three rotation variables r_x, r_y, r_z and three position variables X_{laser}, Y_{laser}, Z_{laser}. Using ${}^{end1}_{laser}T$, the homogeneous transformation matrix from {base1} to {laser} can be obtained as

$$ {}^{base1}_{laser}T = {}^{base1}_{end1}T \cdot {}^{end1}_{laser}T \tag{5} $$

where ${}^{base1}_{end1}T$ represents the robot forward kinematics model. Using the D-H (Denavit-Hartenberg) parameters provided by the robot manufacturer, ${}^{base1}_{end1}T$ can be constructed.

According to the mechanical parameters of the LK-H050 laser sensor, the sensor's zero point is located 50 mm away from the light-emitting port. If the direction away from the light-emitting port is considered positive, the sensor's return value d represents the distance from the zero point to the intersection of the laser and the contact surface. As illustrated in Fig. 5, the measured point can be described as

https://doi.org/10.1017/S0263574725000384 Published online by Cambridge University Press

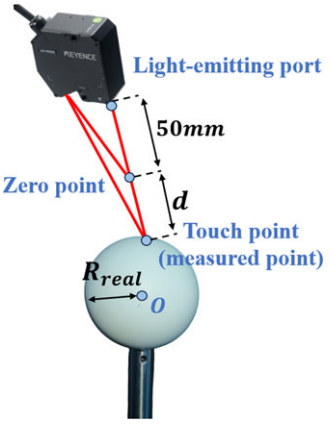


Figure 5. *The model of the laser sensor and a standard sphere.*

$$ {}^{base1}_{touch}T = {}^{base1}_{laser}T \cdot {}^{laser}_{touch}T_P \tag{6} $$

where ${}^{laser}_{touch}T_P$ represents the position of the measured point in {laser} and can be expressed as

$$ {}^{laser}_{touch}T_P = \begin{bmatrix} 1 & 0 & 0 & 0 \\ 0 & 1 & 0 & 0 \\ 0 & 0 & 1 & 50+d \\ 0 & 0 & 0 & 1 \end{bmatrix} \tag{7} $$

Thus, the position of the measured point in the base coordinate system of the measurement robot, ${}^{base1}_{touch}P = [x, y, z]^T$, can be obtained, which is contained within ${}^{base1}_{touch}T$.

3.2 The theoretical kinematic model of the machining robot

Figure 6 shows the machining robot. Corresponding coordinate systems are established for its base, flange, ball-end milling cutter, and workpiece. {base2} denotes the base coordinate system of the machining robot. {end2} refers to the flange coordinate system of the measurement robot. {tool} represents the coordinate system of the ball-end milling cutter, with its origin located at the tool tip. {work} corresponds to the workpiece coordinate system and matches {work} in Section 3.1. Figure 7 shows the logical relationships between the established coordinate systems.

Since the constructure of the machining robot are identical to that of the measurement robot, the homogeneous transformation matrices between the coordinate systems are familiar. The process for obtaining the target matrices ${}^{base2}_{work}T$ and ${}^{base2}_{end2}T$ is also identical to that of the measurement robot. The matrix ${}^{end2}_{tool}T$ represents the homogeneous transformation matrix of {tool} relative to {end2} and can be expressed as

$$ {}^{end2}_{tool}T = {}^{end2}_{tool}T_P \cdot Rot_z(r'_z) \cdot Rot_y(r'_y) \cdot Rot_x(r'_x) \tag{8} $$

In this equation, ${}^{end2}_{tool}T_P$ represents the position of the tool end in {end2}, expressed by the following homogeneous transformation matrix:

$$ {}^{end2}_{tool}T_P = \begin{bmatrix} 1 & 0 & 0 & X_{tool} \\ 0 & 1 & 0 & Y_{tool} \\ 0 & 0 & 1 & Z_{tool} \\ 0 & 0 & 0 & 0 \end{bmatrix} \tag{9} $$

Equations and involve three rotational variables, r'_x, r'_x, r'_z and three positional variables, X_{tool}, Y_{tool}, and Z_{tool}. Consequently, the position of the tool tip in {base2} is denoted as ${}^{base2}_{tool}P = [x, y, z]^T$. This position

https://doi.org/10.1017/S0263574725000384 Published online by Cambridge University Press

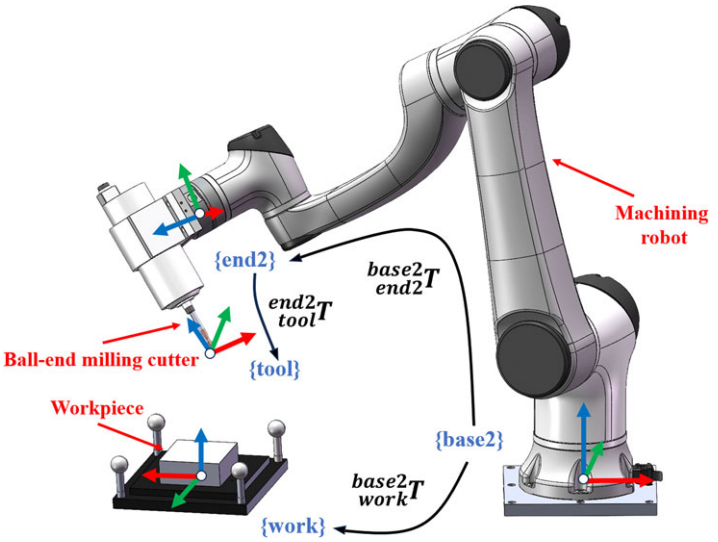


Figure 6. *The theoretical kinematic model of the measurement robot.*

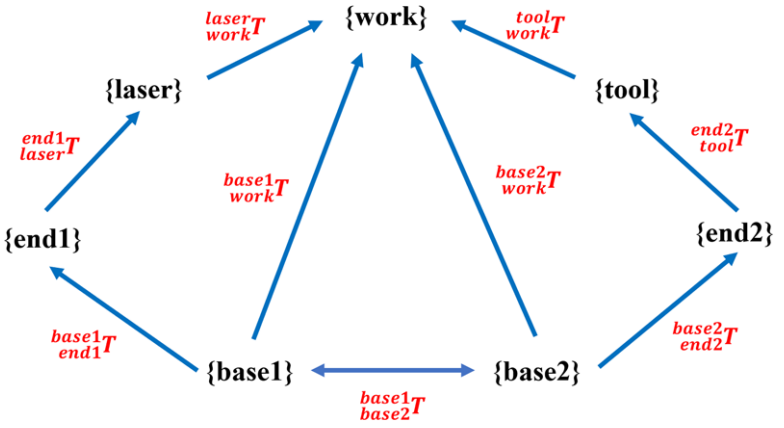


Figure 7. *The logical relationships between the established coordinate systems.*

is encapsulated within the matrix ${}^{base2}_{tool}T$, which is calculated using the following formula:

$$ {}^{base2}_{tool}T = {}^{base2}_{end2}T \cdot {}^{end2}_{tool}T \tag{10} $$

3.3 The theoretical kinematic model of the dual-robot system

The schematic diagram illustrating the logical relationships between the established coordinate systems is as follows:

Based on the established kinematic relationships of each robot, it is necessary to obtain the kinematic relationship between the robots, thus forming a dual-robot system. The matrix ${}^{base2}_{base1}T$ defines the relationship between the base coordinate systems of the measurement robot and machining robot. Considering that both robots share a common workpiece coordinate system, the matrix ${}^{base2}_{base1}T$ can be expressed as

$$ {}^{base2}_{base1}T = {}^{base2}_{work}T \cdot \left({}^{base1}_{work}T\right)^{-1} \tag{11} $$

${}^{base1}_{work}T$ and ${}^{base2}_{work}T$ denote the calibrated homogeneous transformation matrices of the {work} relative to {base1} and {base2}, respectively.

https://doi.org/10.1017/S0263574725000384 Published online by Cambridge University Press

4. Calibration of the dual-robot system and the machining stage

In a dual-robot system, the deviation between the theoretical and actual relative positions of the two robot coordinate systems affects the machining accuracy during the machining stage. Therefore, during the calibration stage, kinematic calibration must be performed separately for the measurement robot and machining robot. By using the shared workpiece coordinate system, the calibrated spatial relationship between the measurement and machining robots can be determined. During the actual machining process, due to the complexity of the workpiece, the position and orientation of the fixture in the machining area often require adjustments. Therefore, during the machining stage, the workpiece coordinate system needs to be re-measured and recalibrated for each machining instance.

4.1 The calibration stage

As both robots are of the same model, the following discussion will focus on the calibration process of the measurement robot. The same method could be applied for optimizing the model of the machining robot.

The homogeneous transformation matrix ${}^{base1}_{end1}T$ is obtained by multiplying six individual transformation matrices. According to the D-H parameter, each transformation matrix ${}^{i-1}_{i}T$ contains four variables $(\alpha_{i-1}, a_{i-1}, d_i, \theta_i)$, which can be represented as

$$ {}^{i-1}_{i}T = Rot_x(\alpha_{i-1}) \cdot Trans_x(a_{i-1}) \cdot Rot_z(\theta_i + q_i) \cdot Trans_z(d_i) \tag{12} $$

where q_i represents the drive joint angle. By adding deviation quantities $\Delta\alpha_{i-1}$, Δa_{i-1}, Δd_i, and $\Delta\theta_i$ to their theoretical values, we obtain the error-considered coordinate transformation matrix ${}^{i-1}_{i}T_e$, as expressed in the following equation:

$$ {}^{i-1}_{i}T_e = Rot_x(\alpha_{i-1} + \Delta\alpha_{i-1}) \cdot Trans_x(a_{i-1} + \Delta a_{i-1}) \cdot Rot_z(\theta_i + \Delta\theta_i + q_i) \cdot Trans_z(d_i + \Delta d_i) \tag{13} $$

Thus, the overall kinematic model of the robot is represented by the following formula:

$$ {}^{base1}_{end1}T_e = {}^{0}_{6}T_e = {}^{0}_{1}T_e \cdot {}^{1}_{2}T_e \cdot {}^{2}_{3}T_e \cdot {}^{3}_{4}T_e \cdot {}^{4}_{5}T_e \cdot {}^{5}_{6}T_e \tag{14} $$

Considering position-pose errors of ${}^{end1}_{laser}T$, the ${}^{end1}_{laser}T_e$ is established and is expressed by adding deviation quantities Δr_x, Δr_y, Δr_z, ΔX_{laser}, ΔY_{laser}, and ΔZ_{laser} as follows:

$$ {}^{end1}_{laser}T_e = {}^{end1}_{laser}T_P_e \cdot Rot_z(r_z + \Delta r_z) \cdot Rot_y(r_y + \Delta r_y) \cdot Rot_x(r_x + \Delta r_x) \tag{15} $$

where ${}^{end1}_{laser}T_P_e$ can be expressed as

$$ {}^{end1}_{laser}T_P_e = \begin{bmatrix} 1 & 0 & 0 & X_{laser} + \Delta X_{laser} \\ 0 & 1 & 0 & Y_{laser} + \Delta Y_{laser} \\ 0 & 0 & 1 & Z_{laser} + \Delta Z_{laser} \\ 0 & 0 & 0 & 1 \end{bmatrix} \tag{16} $$

Considering the deviation quantities, the coordinates of the measurement point in {base1} are given by

$$ {}^{base1}_{touch}T_P_e = {}^{base1}_{end1}T_e \cdot {}^{end1}_{laser}T_e \cdot {}^{laser}_{touch}T_P \tag{17} $$

${}^{base1}_{touch}T_P_e$ denotes the homogeneous transformation matrix representing the position of the measured point in {base1}. The coordinate vector of ${}^{base1}_{touch}T_P_e$ is denoted as ${}^{base1}_{touch}P_e = [x, y, z]^T$.

The error-considered transformation matrix ${}^{base1}_{work}T_e$ from {base1} to {work} is established by introducing deviation quantities ΔR_x, ΔR_y, ΔR_z, ΔX_{work}, ΔY_{work}, and ΔZ_{work} into the six variables R_x,R_y, R_z, X_{work}, Y_{work}, and Z_{work}. This results in the error-considered transformation matrix ${}^{base1}_{work}T_e$:

$$ {}^{base1}_{work}T_e = {}^{base1}_{work}T_P_e \cdot Rot_z(R_z + \Delta R_z) \cdot Rot_y(R_y + \Delta R_y) \cdot Rot_x(R_x + \Delta R_x) \tag{18} $$

https://doi.org/10.1017/S0263574725000384 Published online by Cambridge University Press

In this equation, ${}^{base1}_{work}T_P_e$ can be expressed as

$$ {}^{base1}_{work}T_P_e = \begin{bmatrix} 1 & 0 & 0 & X_{work} + \Delta X_{work} \\ 0 & 1 & 0 & Y_{work} + \Delta Y_{work} \\ 0 & 0 & 1 & Z_{work} + \Delta Z_{work} \\ 0 & 0 & 0 & 1 \end{bmatrix} \tag{19} $$

Due to the high assembly accuracy between the standard sphere and the workpiece fixture, there is no need to introduce deviation quantities in the matrix ${}^{work}_{ball}T_O$, which represents the coordinates of the standard sphere center in {work}. Thus, ${}^{work}_{ball}T_O$ can be expressed as

$$ {}^{work}_{ball}T_O = \begin{bmatrix} 1 & 0 & 0 & X_{ball} \\ 0 & 1 & 0 & Y_{ball} \\ 0 & 0 & 1 & Z_{ball} \\ 0 & 0 & 0 & 1 \end{bmatrix} \tag{20} $$

Based on the relationship between {work} and {base1}, the homogeneous transformation matrix for the center of the standard sphere relative to {base1} can be obtained:

$$ {}^{base1}_{ball}T_O_e = {}^{base1}_{work}T_e \cdot {}^{work}_{ball}T_O \tag{21} $$

${}^{base1}_{ball}T_O_e$ denotes the homogeneous transformation matrix representing the position of the sphere center in {base1}. The coordinate vector of ${}^{base1}_{ball}T_O_e$ is denoted as ${}^{base1}_{ball}O_e = [x, y, z]^T$.

Therefore, in {base1}, the coordinates of the measured point (i.e., the contact point on the sphere surface where the laser line intersects) ${}^{base1}_{touch}P_e$ and the position coordinates of the sphere center ${}^{base1}_{ball}O_e$ are obtained. The distance between the measured point and the sphere center is denoted as $R_{measured}$, which can be expressed as

$$ R_{measured} = \left\| {}^{base1}_{touch}P_e - {}^{base1}_{ball}O_e \right\| \tag{22} $$

$R_{measured}$ represents the actual value of the radius measured by measurement robot and R_{real} represents the real value of the radius of the standard spheres provided by manufacturer. Theoretically, $R_{measured}$ and R_{real} should be equal. However, due to deviations in the kinematic model of the robot, $R_{measured}$ may not match R_{real}. Thus, the deviation between $R_{measured}$ and R_{real} can be used as an optimization target to adjust the constructed error-considered kinematic model. When the difference between $R_{measured}$ and R_{real} is minimized, the accuracy of the corresponding 36 deviation quantities is improved. The specific procedure is as follows:

In this study, n sets of measurement data can be obtained by measuring the standard spheres, with each set containing values for 6 robot joint angles and d. For each set of data, a deviation function $f_i (i \in [1, n], i \in N)$ can be derived based on 36 decision variables, expressed as follows:

$$ f_i = (R_{i,measured} - R_{real})^2 \tag{23} $$

$R_{i,measured}$ represents the radius value calculated based on the ith dataset. The objective function G can be expressed as

$$ G = \frac{1}{n} \sum_{i=1}^{n} f_i \tag{24} $$

The final nonlinear optimization problem can be expressed as

$$ min G(\boldsymbol{x}); s.t. \begin{cases} x_{i,\min} \le x_i \le x_{i,\max} \\ i = 1, 2, 3, \ldots, 36 \end{cases} \tag{25} $$

In the formula above, $\boldsymbol{x} = [x_1, x_2, \ldots, x_{36}]^T \in R^{36}$ represents decision variables, which are four deviation quantities ($\Delta\alpha_{i-1}$, Δa_{i-1}, Δd_i, $\Delta\theta_i$) for each joint of the robot, six deviation quantities (Δr_x, Δr_y, Δr_z, ΔX_{laser}, ΔY_{laser}, ΔZ_{laser}) for the position and pose of the laser sensor coordinate system, and another

https://doi.org/10.1017/S0263574725000384 Published online by Cambridge University Press

six deviation quantities (ΔR_x, ΔR_y, ΔR_z, ΔX_{work}, ΔY_{work}, ΔZ_{work}) for the position and pose of the workpiece coordinate system. $x_{i,min}$ and $x_{i,max}$ denote the lower and upper bounds of x_i, respectively. These bounds can be assigned appropriate values based on theoretical estimates of the error.

The optimization problem involves 36 variables, resulting in a high-dimensional optimization problem that requires an appropriate meta-heuristic algorithm to effectively avoid local optima. In this paper, the EEFO algorithm [30] has been selected for this optimization. The EEFO algorithm is a nature-inspired swarm intelligence optimization technique based on the collective foraging behavior of electric eels. By clustering and driving prey into a "bait ball" for a high-pressure attack, eels optimize their hunting efficiency. This strategy inspires the development of the EEFO algorithm to enhance optimization performance. In this study, the algorithm will search within this range to find the vector $\boldsymbol{x}$ that minimizes G.

4.2 The machining stage

In machining stage, the workpiece coordinate system needs to be adjusted for each specific machining instance. Therefore, in each machining instance, the measurement robot is employed to measure the four standard spheres around the workpiece and obtain the homogeneous transformation matrix ${}^{base1}_{work'}T$. Using ${}^{base2}_{base1}T$ obtained in the calibration stage, ${}^{base2}_{work'}T$ can be derived.

Since the kinematic parameters of the measurement robot have already been calibrated during the calibration stage, constructing the objective function H only requires introducing six deviation quantities ($\Delta R_{x'}$, $\Delta R_{y'}$, $\Delta R_{z'}$, $\Delta X_{work'}$, $\Delta Y_{work'}$, and $\Delta Z_{work'}$) for the position and pose of the adjusted workpiece coordinate system. The modeling approach for the objective function is consistent with Section 4.1. The objective function H can be expressed as

$$H = \frac{1}{n}\sum_{i=1}^{n} f_i \tag{26}$$

The final nonlinear optimization problem can be expressed as

$$minH(\boldsymbol{x}); s.t. \begin{cases} x_{i,\min} \le x_i \le x_{i,\max} \\ i = 1, 2, 3, 4, 5, 6 \end{cases} \tag{27}$$

By applying the EEFO algorithm, the six deviation quantities can be resolved, yielding the transformation matrix ${}^{base1}_{work'}T$. Subsequently, ${}^{base2}_{work'}T$ is derived using the following equation:

$${}^{base2}_{work'}T = {}^{base2}_{base1}T \cdot {}^{base1}_{work'}T \tag{28}$$

By using Eq. (28), the surface machining trajectory in work space can be transformed into the machining robot base system to perform high-precision machining. If another surface part needs to be machined, it is only necessary to repeat the steps in this section to obtain the new fixture position.

5. Experiments and results

5.1 Verification of measurement experiments

The constructed dual-robot system for measurement and machining is illustrated in Fig. 8. By using the proposed method, an objective function as shown in Eq. (24) is formulated, optimizing structural parameters of the measurement-machining system.

By employing the optimization method proposed in this study, the value of the objective function G for the measurement robot is reduced to 1.250, resulting in a minimized sphere radius deviation of 0.039 mm. Similarly, the value of the objective function G for the machining robot is reduced to 4.025, resulting in a minimized sphere radius deviation of 0.069 mm. Tables I and II list the optimization results of kinematic parameters deviation for measurement robot and machining robot. Tables III and IV list

https://doi.org/10.1017/S0263574725000384 Published online by Cambridge University Press

Table I. *EEFO-optimized results of kinematic parameters deviation for measurement robot.*

Link of the robot	$\Delta\alpha_{i-1}/^\circ$	Δa_{i-1}/mm	Δd_i/mm	$\Delta\theta_i/^\circ$
Link1	−1.009	1.656	−3.706	1.067
Link2	0.191	−1.428	−2.068	−0.180
Link3	−0.214	0.440	−0.156	0.256
Link4	0.116	−3.033	0.075	−2.241
Link5	0.104	1.265	−1.623	0.372
Link6	−0.502	−1.706	0.651	4.702

Table II. *EEFO-optimized results of kinematic parameters deviation for machining robot.*

Link of the robot	$\Delta\alpha_{i-1}/^\circ$	Δa_{i-1}/mm	Δd_i/mm	$\Delta\theta_i/^\circ$
Link1	−1.854	0.855	−2.480	0.552
Link2	0.017	1.503	−2.185	−0.020
Link3	−0.164	0.218	5.374	0.436
Link4	0.695	−1.112	0.655	−0.499
Link5	−0.006	0.276	−2.015	0.871
Link6	−0.433	−4.239	−1.271	1.070

Table III. *EEFO-optimized results of laser sensor coordinate system deviation.*

Robot	$\Delta r_x/^\circ$	$\Delta r_y/^\circ$	$\Delta r_z/^\circ$	ΔX_{laser}/mm	ΔY_{laser}/mm	ΔZ_{laser}/mm
Measurementrobot	3.274	−2.892	−3.274	6.035	−1.410	0.589
Machiningrobot	−1.623	−0.188	1.520	−0.384	−0.704	−1.283

Table IV. *EEFO-optimized results of workpiece coordinate system deviation.*

Robot	$\Delta R_x/^\circ$	$\Delta R_y/^\circ$	$\Delta R_z/^\circ$	ΔX_{work}/mm	ΔY_{work}/mm	ΔZ_{work}/mm
Measurementrobot	−1.129	0.317	0.890	−1.032	−0.710	−3.204
Machiningrobot	−1.577	−0.009	0.333	−0.460	6.160	−4.735

the optimization results of laser sensor coordinate system deviation and workpiece coordinate system deviation for each robot.

It should be noted that these parameters are specifically designed to optimize accuracy within a localized region. As the robot's end-effector moves further away from the workpiece coordinate system, the positioning error may increase. However, this characteristic is advantageous, as these parameters are not intended to reflect the true structural configuration of the robot. Instead, they function as compensation parameters tailored to reduce errors within the specific local space where machining occurs. Since the machining trajectory is confined to a local area, focusing on enhancing local accuracy is far more meaningful than striving for global precision. This approach ensures higher accuracy and efficiency in machining applications, where localized accuracy directly impacts the quality of the machining.

5.2 Calibration accuracy verification experiment

To validate the calibration accuracy of the dual-robot system, measurements and analyses of the standard spheres are conducted both within and outside the valid region. Five positions (Position **A**∼**E**) are set

https://doi.org/10.1017/S0263574725000384 Published online by Cambridge University Press



Figure 8. *The dual-robot system and the calibration process.*

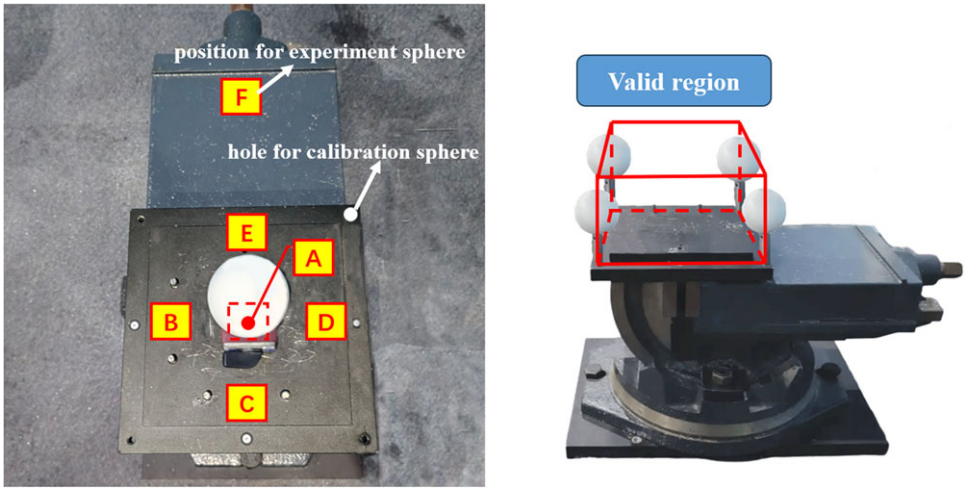


Figure 9. *Settings of test positions.*

within the calibration area for placing the standard spheres, with an additional position (Position **F**) set outside the effective calibration area. The placement of the standard spheres is shown in Fig. 9.

During the experiment, the measurement robot scans the standard spheres to capture a considerable number of points. Using the calibrated forward kinematics model of the measurement robot, the positions of the measured points in {base1} are obtained, and the position of the sphere center ${}^{base1}_{ball}O$ can be calculated using a fitting algorithm. Then, the position of the sphere center in {base2} ${}^{base2}_{ball}O_{cnv} = [x, y, z]^T$ can be converted from ${}^{base1}_{ball}O$:

$$ {}^{base2}_{ball}O_{cnv} = {}^{base2}_{base1}T \cdot {}^{base1}_{ball}O \tag{29} $$

A laser sensor is mounted on the machining robot to measure the same sphere, thereby directly obtaining the position data ${}^{base2}_{touch}P_i$ of the standard sphere in {base2}. Theoretically, the distance $\| {}^{base2}_{touch}P_i - {}^{base2}_{ball}O_{cnv} \|$ between the measured point and the sphere center should equal the actual radius R_{real}. However, due to the deviations in the kinematic model, a discrepancy exists between this distance and R_{real}, which reflects the positioning accuracy error. The error at each point can be calculated by the following formula:

$$ \delta_i = \left| \left\| {}^{base2}_{touch}P_i - {}^{base2}_{ball}O_{cnv} \right\| - R_{real} \right| = \left| \left\| {}^{base2}_{touch}P_i - {}^{base2}_{base1}T \cdot {}^{base1}_{ball}O \right\| - R_{real} \right| \tag{30} $$

https://doi.org/10.1017/S0263574725000384 Published online by Cambridge University Press

Table V. *The average positioning error of the six positions.*

Position	**A**	**B**	**C**	**D**	**E**	**F**
E_{th}/mm	3.2315	3.3698	3.3474	3.1752	3.2272	4.1403
E_{ca}/mm	0.4287	0.3993	0.4758	0.6095	0.3416	1.7689
Ratio/%	86.7	88.2	85.8	80.8	89.4	57.3

Table VI. *The maximal positioning error of the six positions.*

Position	**A**	**B**	**C**	**D**	**E**	**F**
E_{th}/mm	7.4329	7.6649	7.6025	7.3151	7.3728	8.9677
E_{ca}/mm	0.7879	0.8011	0.8622	0.9214	0.7333	3.5178
Ratio/%	89.4	89.6	88.7	87.4	90.1	60.8

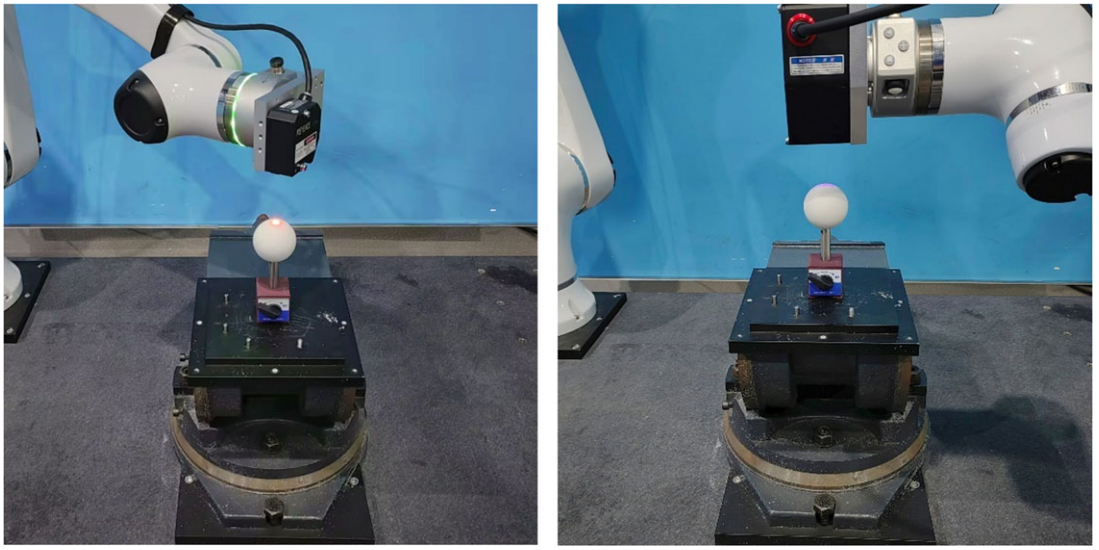


Figure 10. *The procedure of the calibration accuracy verification experiment.*

δ_i represents the localization error of the ith sampling point. In this experiment, each sphere is sampled at 210 points, thus $i \in [1, 210]$, $i \in Z$. ${}^{base2}_{touch}P_i$ represents the coordinates of each sampling point in {base2}. Figure 10 shows the procedure of the calibration accuracy verification experiment.

Since the calculation of δ_i requires the kinematic model of both robots, using different kinematic models will yield different error values. In this study, both the theoretical and calibrated kinematic models are used in Eq. 30 for comparison. The average error values for the measurements at six different positions (Position **A**∼**F**) are shown in Fig. 11. Table V lists the average positioning error of the six positions, and Table VI lists the maximal positioning error of the six positions.

From Tables V, VI, and Fig. 11, it can be summarized that the deviation values obtained using the theoretical kinematic model are significantly higher than those using the calibrated kinematic model, both for average and maximal deviations, whether inside or outside the region. This result demonstrates the effectiveness of the calibration algorithm in improving accuracy. At the same time, for the standard spheres inside the region (Position **A**∼**E**), the average positioning error after calibration is less than 0.7 mm, and the maximal error is less than 1 mm. For the standard spheres outside the region (Position **F**), the average positioning error after calibration is 1.7689 mm, and the maximal positioning error is 3.5178 mm. This indicates that the calibration algorithm has a far greater improvement effect within the local region than outside.

https://doi.org/10.1017/S0263574725000384 Published online by Cambridge University Press

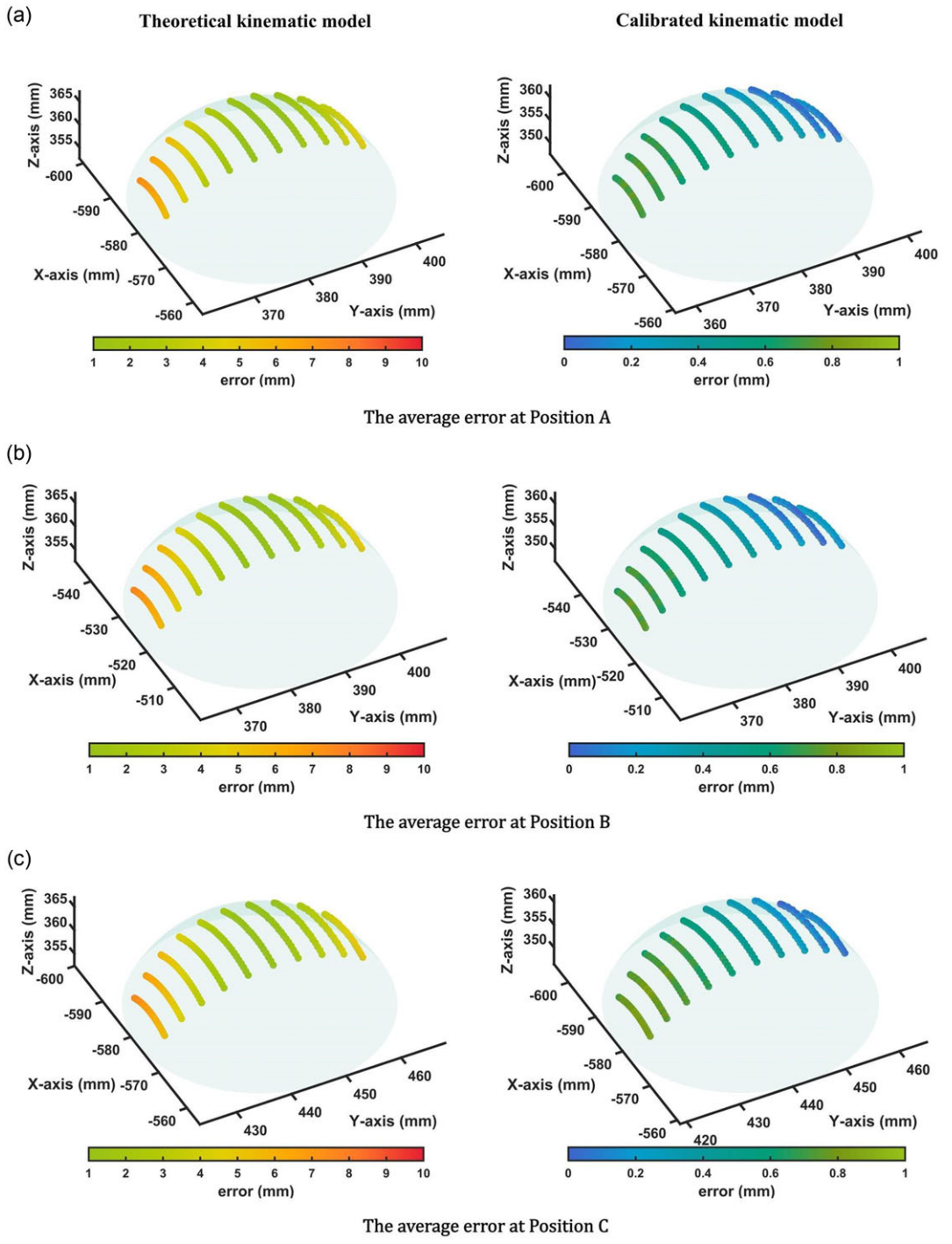
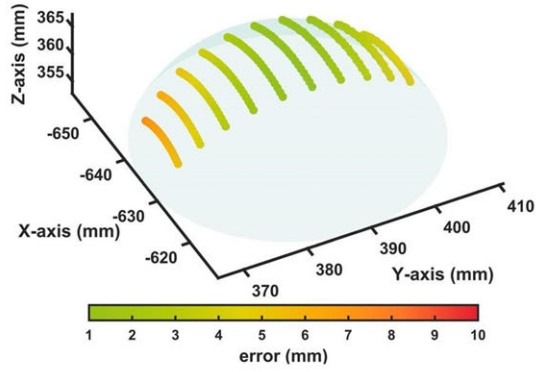
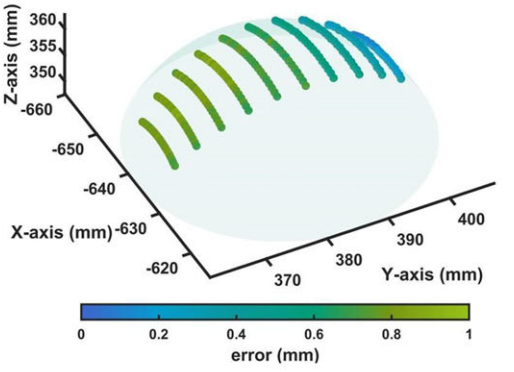


Figure 11. *Comparison of positioning errors of six test positions.*

https://doi.org/10.1017/S0263574725000384 Published online by Cambridge University Press

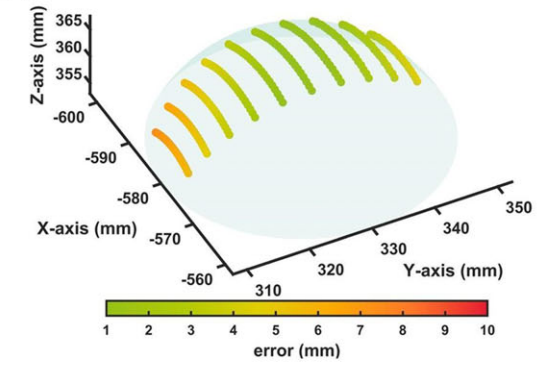
(d)

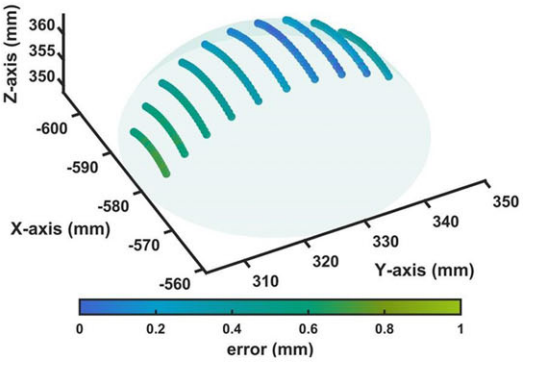




The average error at Position D

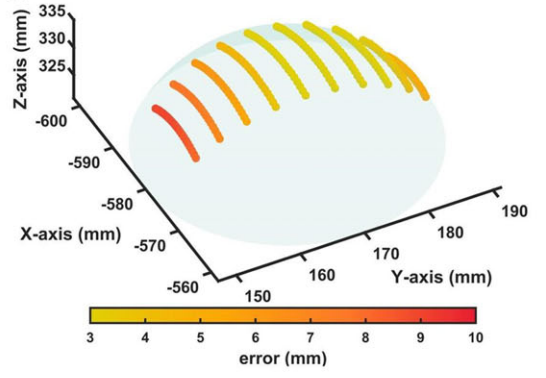
(e)

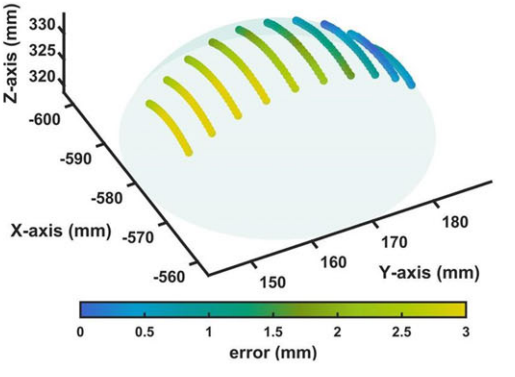




The average error at Position E

(f)





The average error at Position F

Figure 11. *(Continued)*

https://doi.org/10.1017/S0263574725000384 Published online by Cambridge University Press

Table VII. *SQP-optimized results of kinematic parameters deviation for measurement robot.*

Link of the robot	$\Delta\alpha_{i-1}/^\circ$	Δa_{i-1}/mm	Δd_i/mm	$\Delta\theta_i/^\circ$
Link1	141.483	−158.916	64.521	−204.329
Link2	−72.087	−605.627	−29.260	−177.492
Link3	−40.179	−102.848	−75.130	−395.487
Link4	−74.199	20.712	51.904	−146.415
Link5	90.716	−90.077	−39.965	344.405
Link6	110.654	−137.337	−118.795	−208.315

Table VIII. *SQP-optimized results of kinematic parameters deviation for machining robot.*

Link of the robot	$\Delta\alpha_{i-1}/^\circ$	Δa_{i-1}/mm	Δd_i/mm	$\Delta\theta_i/^\circ$
Link1	21.055	−168.188	34.292	17.963
Link2	−28.054	−217.979	21.553	214.572
Link3	21.663	−17.862	−54.832	−58.583
Link4	−31.970	59.293	45.303	−248.814
Link5	−11.848	−134.579	118.762	−42.976
Link6	−14.969	96.678	−128.295	−145.246

The tables also present the accuracy improvement ratio for both inside and outside the region, *Ratio* in Tables V and VI is defined as

$$Ratio = \left|1 - \frac{E_{ca}}{E_{th}}\right| \times 100\% \tag{31}$$

where E_{th} represents the positioning error calculated with the theoretical kinematic model, and E_{ca} represents the positioning error calculated with the calibrated kinematic model. As shown in the tables, the accuracy improvement ratio for positions inside the region is higher than that for positions outside the region. This further confirms that the calibration algorithm effect on accuracy improvement is more significant within the local region than outside it.

5.3 Algorithm comparison experiment

Due to the nonlinear, high-dimensional, and constrained nature of the dual-robot system calibration problem, traditional gradient-based methods are highly sensitive to initial values, where small deviations may lead to overfitting and cause the algorithm to become trapped in a local optimum. Given that meta-heuristic optimization algorithms possess strong global search capabilities and can better handle such problems, this paper adopts the EEFO algorithm to avoid overfitting and enhance the calibration accuracy. To validate its effectiveness and necessity, this section employs a commonly used gradient-based method, the sequential quadratic programming algorithm (SQP), for calibrating the dual-robot system, and compares the results with those obtained using the EEFO algorithm in Sections 5.1 and 5.2. The relevant results are listed in Tables VII–X.

By employing the SQP algorithm, the value of the objective function G for the measurement robot is reduced to 58691.815 (EEFO: 1.250), which means the minimized sphere radius deviation is 8.359 mm (EEFO: 0.039 mm). Similarly, the value of the objective function G for the machining robot is reduced to 51258.488 (EEFO: 4.025), and the minimized sphere radius deviation is 7.211 mm (EEFO: 0.069 mm). It can be observed from the objective function values that the value obtained by the SQP algorithm is significantly greater than that obtained by the EEFO algorithm. To further demonstrate the robustness of

https://doi.org/10.1017/S0263574725000384 Published online by Cambridge University Press

Table IX. *SQP-optimized results of laser sensor coordinate system deviation.*

Robot	$\Delta r_x/^\circ$	$\Delta r_y/^\circ$	$\Delta r_z/^\circ$	ΔX_{laser}/mm	ΔY_{laser}/mm	ΔZ_{laser}/mm
Measurementrobot	66.587	295.867	−29.337	−9.130	−37.965	−210.003
Machiningrobot	−8.707	20.822	103.206	51.195	−120.420	−143.928

Table X. *SQP-optimized results of workpiece coordinate system deviation.*

Robot	$\Delta R_x/^\circ$	$\Delta R_y/^\circ$	$\Delta R_z/^\circ$	ΔX_{work}/mm	ΔY_{work}/mm	ΔZ_{work}/mm
Measurementrobot	138.537	−27.830	−11.499	161.301	−113.038	18.294
Machiningrobot	15.615	−32.248	37.741	169.391	−407.495	160.663

Table XI. *Mean error and error variance of two algorithms.*

Algorithm	**Mean error/mm**	**Error variance/mm^2**
EEFO	7.878×10^{-2}	4.890×10^{-5}
SQP	1.619	2.510

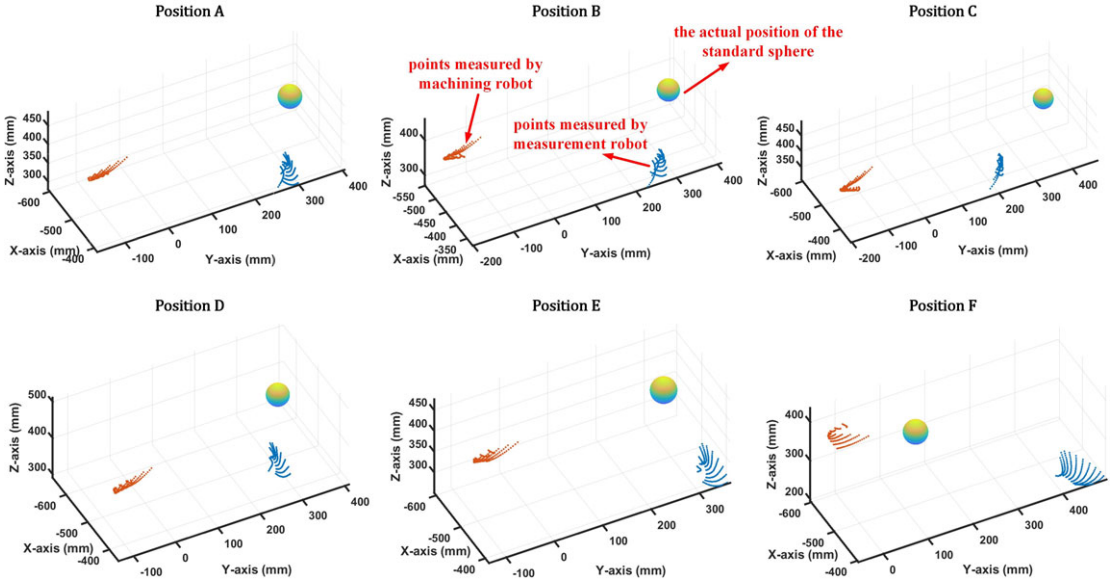


Figure 12. *Measured points under SQP-calibration and fitted spheres under EEFO-calibration.*

the EEFO algorithm, 10 comparative experiments were conducted with different initial values, and the results of the two algorithms are compared in Table XI. Since the models of both robots are identical, it is sufficient to validate the robustness of the algorithm on one robot (the machining side).

To further illustrate the error caused by the SQP algorithm, measurements are conducted on the same standard sphere using both robots, following the same experimental procedure as described in Section 5.2. The point cloud is reconstructed based on the SQP-calibrated model. The experimental results are shown in Fig. 12. In the figure, the red point cloud corresponds to the data collected by the machining robot, while the blue point cloud is acquired by the measurement robot. It can be observed that the reconstructed point cloud exhibits a significant deviation from the actual position of the standard sphere. Moreover, the reconstructed point cloud has lost the spherical characteristics that the actual point cloud should exhibit, making it impossible to fit a sphere as the actual point cloud could.

https://doi.org/10.1017/S0263574725000384 Published online by Cambridge University Press

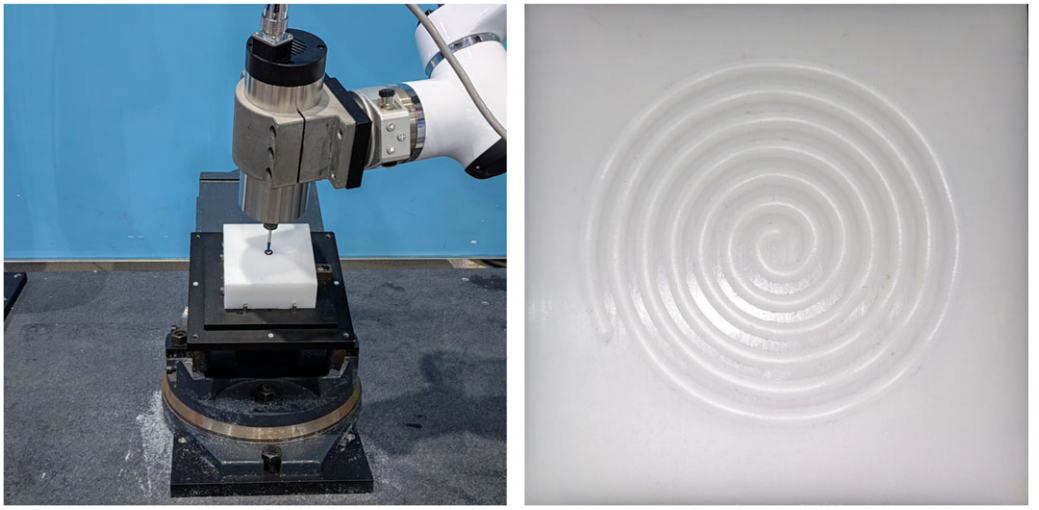


Figure 13. *The machining process and results of the spiral line.*

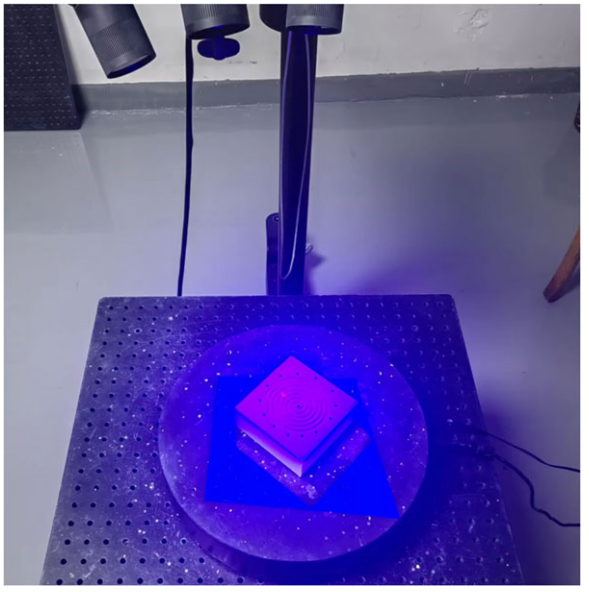


Figure 14. *The process of precision measurement.*

5.4 Verification of the spiral line machining experiment

To validate the trajectory accuracy of the dual-robot calibration, this study machines a portion of the Archimedean spiral. The fixture is rotated to form an angle with the *oxy* plane, and the workpiece is placed in the center of the fixture.

The measurement robot measures four standard spheres around the fixture, from which ${}^{base1}_{work}T$ is derived using the previously mentioned method, and ${}^{base2}_{work}T$ is subsequently obtained using ${}^{base1}_{base2}T$. The machining process is then carried out using the machining robot, with the results displayed in Fig. 13.

To assess the precision of the machined curve, a high-precision 3D scanner, the ATOS Q 12 M model (as shown in Fig. 14), is employed to capture point clouds and evaluate the accuracy of the curve. Measurements indicate that the average error of the spiral line is 0.073 mm. Figure 15 shows the theoretical curve of the Archimedean spiral processed in this experiment, along with the numerical values and distribution of the trajectory errors.

https://doi.org/10.1017/S0263574725000384 Published online by Cambridge University Press

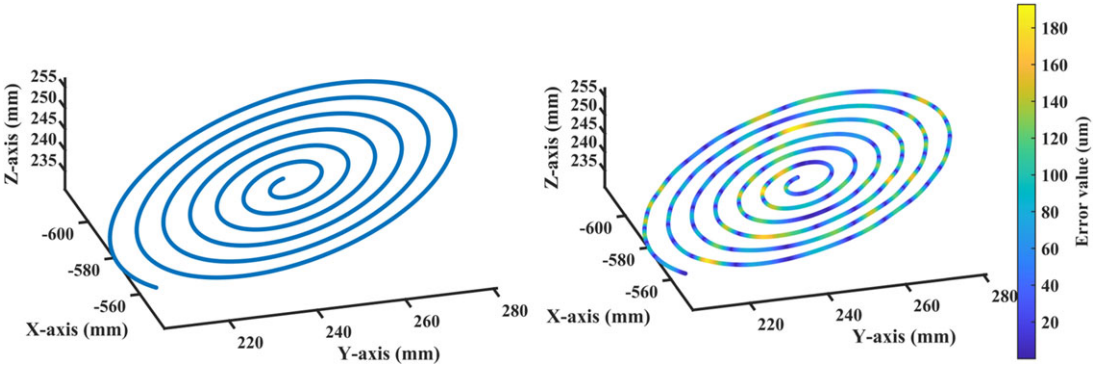


Figure 15. *Theoretical curve diagram and error distribution diagram of the spiral line.*

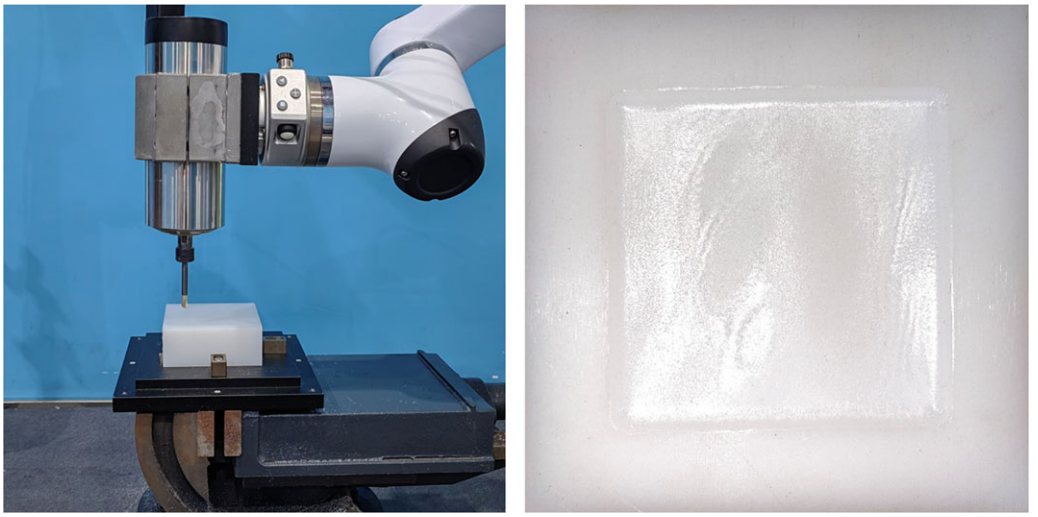


Figure 16. *The machining process and results of the sine surface.*

5.5 Verification of the sine surface machining experiment

To prove the ability of the dual-robot system to accommodate small adjustments in the workspace pose, this study further adjusts the position and pose of the fixture and conducts a surface machining experiment. The fixture is rotated to the position shown in Fig. 16, and the workpiece is placed on the fixture.

The calibration and processing are carried out, resulting in the surface shown in Fig. 16. The accuracy of the processed surface is measured using the same equipment as shown in Section 5.3, and the results are presented in Fig. 17. The experimental results indicate that the average accuracy of the surface machining trajectory is 0.109 mm.

6. Conclusion

This paper presents a method for calibrating a dual-robot system within a localized space, based on the in situ measurement and a meta-heuristic algorithm (EEFO algorithm), to enhance the machining trajectory accuracy in that space. Through this calibration method, the kinematic parameters of the robot can be calibrated within the localized space, ultimately enhancing the positioning accuracy of the end-effector. Consequently, this calibration method is applicable to various operations within this area, such as machining, spraying and assembly, demonstrating its broad applicability. The final experimental results indicate that the trajectory accuracy can reach approximately 0.1 mm, thereby demonstrating the

https://doi.org/10.1017/S0263574725000384 Published online by Cambridge University Press

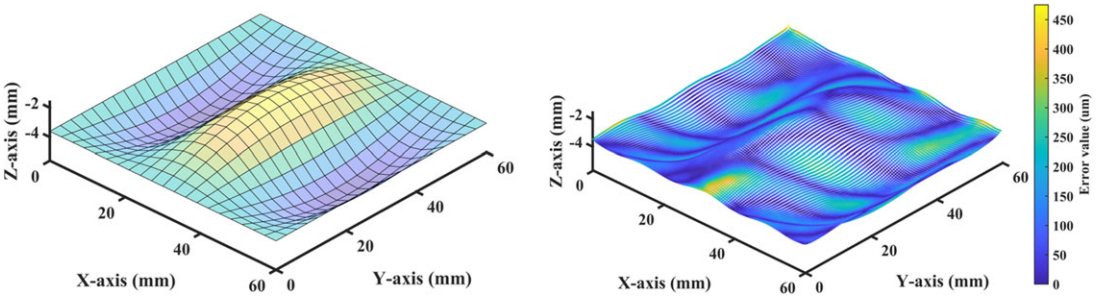


Figure 17. *Theoretical surface diagram and error distribution diagram of the sine surface.*

effectiveness of the proposed method. It should be noted that this paper uses milling experiments for validation; however, the proposed method is not limited to milling and can be extended to robot grinding or robot polishing.

The integrated dual-robot measurement and calibration system proposed in this study assigns the machining and measurement functions to two separate robots, overcoming the problem of increased calibration errors caused by the frequent switching of end effectors in existing single-robot machining systems during the calibration process. Compared with existing dual-robot calibration methods, the proposed method in this paper utilizes a meta-heuristic algorithm, addressing the issue of local minima often encountered in traditional gradient-based calibration techniques. The calibration method proposed in this paper still has limitations in terms of measurement data efficiency. Future work will focus on further investigating ways to improve measurement efficiency and reduce the number of measurement points.

Author contributions. Zhentao Zhang conceived and designed the study. Zhentao Zhang, Guangde Bi, and Jiajing Li conducted data gathering and analyses. Zhentao Zhang wrote the article. Lining Sun and Lei Lu provided practical feedback and guidance throughout the study.

Financial support. This research was supported by the Postdoctoral Science Foundation of China (No.2023M730348) and the Undergraduate Training Program for Innovation and Entrepreneurship, Soochow University (No. 202410285063Z). Thanks for the technical service provided by Han's Robot.

Competing interests. The authors affirm that no conflicts of financial interest or personal relationships exist that could have inappropriately influenced the work presented in this manuscript.

Ethical approval. Not applicable.

References

[1] A. Rosyid, C. Stefanini and B. El-Khasawneh, "A novel walking parallel robot for on-structure three-axis machining of large structures," *J. Mech. Robot.* **15**(6), 061016 (2023).

[2] C. De Benedictis and C. Ferraresi, "Precise positioning in a robotized laser-cutting machine allowed by a three-V-shaped-groove kinematic coupling: A feasibility study," *Robotica* **41**(9), 2703–2712 (2023).

[3] Z. Xie, F. Xie, X.-J. Liu, J. Wang and X. Shen, "Parameter optimization for the driving system of a 5 Degrees-of-freedom parallel machining robot with planar kinematic chains," *J. Mech. Robot.* **11**(4), 410–415 (2019).

[4] R. Li, X. L. Cui, J. C. Lin and Y. H. Zheng, "An attitude measurement method of industrial robots based on the inertial technology," *Robotica* **40**(8), 2909–2931 (2022).

[5] L. Xu, X. Chai and Y. Ding, "Design and analysis of a reconfigurable hybrid robot for machining of large workpieces," *J. Mech. Robot.* **16**(5), 051001 (2023).

[6] J. Wu, Y. Gao, B. B. Zhang and L. P. Wang, "Workspace and dynamic performance evaluation of the parallel manipulators in a spray-painting equipment," *Robot. Cim-INT Manuf.* **44**(1), 199–207 (2017).

[7] J. L. Xiao, S. L. Zhao, H. Guo, T. Huang and B. Lin, "Research on the collaborative machining method for dual-robot mirror milling," *Int. J. Adv. Manuf. Technol.* **105**(10), 4071–4084 (2019).

https://doi.org/10.1017/S0263574725000384 Published online by Cambridge University Press

[8] S. Veeramani and S. Muthuswamy, "Hybrid type multi-robot path planning of a serial manipulator and SwarmItFIX robots in sheet metal milling process," *Complex Intell. Syst.* **8**(4), 2937–2954 (2022).
[9] X. W. Zhao, B. Tao and H. Ding, "Multimobile robot cluster system for robot machining of large-scale workpieces," *IEEE-ASME Trans. Mech.* **27**(1), 561–571 (2022).
[10] J. A. Marvel, R. Bostelman and J. Falco, "Multi-robot assembly strategies and metrics," *ACM Comput. Surv.* **51**(1), 1–32 (2018).
[11] M. Dogar, A. Spielberg, S. Baker and D. Rus, "Multi-robot grasp planning for sequential assembly operations," *Auton. Robot.* **43**(3), 649–664 (2019).
[12] Z. Feng, G. Q. Hu, Y. J. Sun and J. Soon, "An overview of collaborative robotic manipulation in multi-robot systems," *Ann. Rev. Control* **49**(1), 113–127 (2020).
[13] G. Boschetti, M. Bottin, M. Faccio and R. Minto, "Multi-robot multi-operator collaborative assembly systems: A performance evaluation model," *J. Intell. Manuf.* **32**(5), 1455–1470 (2021).
[14] J. Wu, B. B. Zhang, L. P. Wang and G. Yu, "An iterative learning method for realizing accurate dynamic feedforward control of an industrial hybrid robot," *Sci. China Technol. Sci.* **64**(6), 1177–1188 (2021).
[15] A. Maghami and M. Khoshdarregi, "Vision-based target localization and online error correction for high-precision robotic drilling," *Robotica* **42**(9), 3019–3043 (2024).
[16] Y. Tao, S. Chen, H. T. Liu, J. H. Wan, H. X. Wei and T. M. Wang, "Robot hybrid inverse dynamics model compensation method based on the BLL residual prediction algorithm," *Robotica* **1**(1), 1–18 (2024).
[17] J. Wu, T. M. Li, J. S. Wang and L. P. Wang, "Stiffness and natural frequency of a 3-DOF parallel manipulator with consideration of additional leg candidates," *Robot. Auton. Syst.* **61**(8), 868–875 (2013).
[18] J. Wang, L. Wu, M. Q.-H. Meng and H. Ren, Towards simultaneous coordinate calibrations for cooperative multiple robots, 410–415 (2014).
[19] L. Wu, J. L. Wang, L. Qi, K. Y. Wu, H. L. Ren and M. Q. H. Meng, "Simultaneous hand-eye, tool-flange, and robot-robot calibration for comanipulation by solving the AXB = YCZ problem," *IEEE Trans. Robot.* **32**(2), 413–428 (2016).
[20] S. Sui and Y. Ding, "Solving the AXB=YCZ problem for a dual-robot system with geometric calculus," *IEEE Trans. Autom. Sci. Eng.* **21**(3), 4627–4645 (2024).
[21] Y. Qiao, Y. P. Chen, B. Chen and J. M. Xie, "A novel calibration method for multi-robots system utilizing calibration model without nominal kinematic parameters," *Precis. Eng.-J. Int. Soc. Precis. Eng. Nanotechnol.* **50**(1), 211–221 (2017).
[22] A. Nubiola and I. A. Bonev, "Absolute calibration of an ABB IRB. 1600 robot using a laser tracker," *Robot. Cim-INT Manuf.* **29**(1), 236–245 (2013).
[23] X. H. Xu, D. H. Zhu, H. Y. Zhang, S. J. Yan and H. Ding, "TCP-based calibration in robot-assisted belt grinding of aero-engine blades using scanner measurements," *Int J Adv Manuf Tech* **90**(1-4), 635–647 (2017).
[24] X. Wang, W. Ren, K. Wang, J. Liu, J. Lin, J. Feng, J. Zheng and F. Li, "A self-calibration method for robot end-effector using spherical constraints," *Appl. Sci.* **14**(21), 9824 (2024).
[25] M. Dehghani, R. A. McKenzie, R. A. Irani and M. Ahmadi, "Robot-mounted sensing and local calibration for high-accuracy manufacturing," *Robot. Cim-INT Manuf.* **79**(1), 102429 (2023).
[26] T. H. Chen, S. Li, Y. Qiao and X. Luo, "A robust and efficient ensemble of diversified evolutionary computing algorithms for accurate robot calibration," *IEEE Trans. Instrum. Meas.* **73**(1), 1–14 (2024).
[27] H. Q. Cao, H. X. Nguyen, T. N. C. Tran, H. N. Tran and J. W. Jeon, "A robot calibration method using a neural network based on a butterfly and flower pollination algorithm," *IEEE Trans. Ind. Electron.* **69**(4), 3865–3875 (2022).
[28] X. Z. Chen and Q. Zhan, "The kinematic calibration of an industrial robot with an improved beetle swarm optimization algorithm," *IEEE Robot. Autom. Lett.* **7**(2), 4694–4701 (2022).
[29] H. R. Zhong, C. H. Hu, X. Y. Li, L. Gao, B. Zeng and H. Z. Dong, "Kinematic calibration method for a two-segment hydraulic leg based on an improved whale swarm algorithm," *Robot. Cim-INT Manuf.* **59**(1), 361–372 (2019).
[30] W. G. Zhao, L. Y. Wang, Z. X. Zhang, H. G. Fan, J. J. Zhang, S. Mirjalili, N. Khodadadi and Q. J. Cao, "Electric EEL foraging optimization: A new bio-inspired optimizer for engineering applications," *Expert Syst. Appl.* **238**(1), 122200 (2024).

Cite this article: Z. Zhang, G. Bi, J. Li, L. Sun and L. Lu (2025). "Improving machining trajectory accuracy for dual-robot system with in situ laser measurement and meta-heuristic optimization", Robotica **43**, 1491–1511. https://doi.org/10.1017/S0263574725000384

https://doi.org/10.1017/S0263574725000384 Published online by Cambridge University Press